Catalysis Science & Technology

ROYAL SOCIETY OF CHEMISTRY

PAPER

View Article Online
View Journal | View Issue

Cite this: *Catal. Sci. Technol.*, 2025, 15, 7395

Direct dehydrogenation of ethylbenzene over C_{60}–Ni/SiO_2 catalysts: mechanistic insight into C_{60} as a molecular promoter

Kunru Fan,†[ab] Xueya Dai,†[ab] Yunli Bai,[ab] Gang Sun,[b] Xiangjie Zeng[b] and Wei Qi *[ab]

Received 4th September 2025,
Accepted 21st October 2025

DOI: 10.1039/d5cy01075f

rsc.li/catalysis

Extensive research in heterogeneous catalysis has highlighted the potential of non-noble metal catalysts for efficient alkane dehydrogenation. Although Ni species are widely employed for activating C–H bonds, their utilization as active catalysts for alkane dehydrogenation is limited by thermal sintering, coke deposition, and undesired side reactions that compromise the stability and selectivity of the catalyst. This work reports the synthesis of a C_{60}-modified nickel-based catalyst (C_{60}–Ni/SiO_2), which was employed for the direct dehydrogenation (DDH) of ethylbenzene (EB) to styrene (ST). Owing to its tailored electronic structure, the C_{60}–Ni/SiO_2 catalyst reached an ST formation rate of 2.7 mmol g^{-1} h^{-1} while maintaining a selectivity exceeding 99.0%. XRD, Raman, TEM, and XPS characterization revealed that the C_{60} served as an electronic promoter, which decreased the electron density of Ni species without disturbing its crystalline structure. Such modulation of the electronic structure of Ni centers effectively suppresses the cracking side reactions and coke formation, thereby improving both selectivity and stability of the catalyst during EB DDH. The present work introduces a promising Ni-based catalyst for EB dehydrogenation, potentially offering prospects for developing advanced non-noble metal catalysts for alkene production *via* the DDH process.

1. Introduction

Styrene (ST) is considered a key raw material in the modern petrochemical industry and is widely utilized for producing polymers, such as polystyrene and butadiene rubber. It is estimated that global ST production exceeds 30 million tons annually, leading to more than 27 million tons of CO_2 emissions each year.[1] Presently, industrial ST production predominantly relies on the direct dehydrogenation of ethylbenzene (EB DDH) over Fe–K–Cr-based catalysts with co-feeding overheated steam. However, Fe–K–Cr catalysts exhibit several limitations, including the instability of active Fe^{3+} sites, loss and redistribution of potassium promoters, and rapid deactivation caused by coke deposition.[2–4] Moreover, a significant excess of steam used in DDH normally results in substantial energy consumption.[5] Therefore, the development of novel, active, and coke-resistant catalysts that can operate with reduced steam consumption or even under steam-free conditions is crucial for improving the energy efficiency of ST production.

Ni-based catalysts have demonstrated remarkable performance in diverse catalytic reactions, including steam reforming,[6,7] the water–gas shift reaction,[8,9] and biomass gasification.[10] As a non-noble metal, Ni has great advantages in terms of low cost and ease of preparation. Recently, Ni-based catalysts have been extensively applied in methane reforming, demonstrating excellent C–H bond activation ability.[11–14] However, Ni-based materials have been rarely applied as catalysts for EB DDH, since Ni species tend to promote both C–H and C–C bond activation due to their strong adsorption capacity of both EB and ST, which accelerates coke formation.[15–17] As a result, the rapid catalyst deactivation accompanied by diminished ST selectivity is commonly observed. A major challenge in solving this problem is that Ni species exhibit high electron density, which facilitates the strong metal–π interactions with aromatic compounds such as benzene. These interactions significantly alter the electron density distribution within the aromatic ring, thereby reducing the activation barriers for undesirable side reactions, including ring opening, cracking, and polymerization.[18,19] These parasitic reactions are acknowledged as primary pathways for the coke generation, which in turn deactivates the catalyst and diminishes both the efficiency and stability of the reaction system. Recent studies have shown increasing efforts in exploring the incorporation of metallic promoters or elemental doping as effective strategies to engineer the electronic structure of Ni

[a] *School of Materials Science and Engineering, University of Science and Technology of China, Shenyang, Liaoning, 110016, P. R. China*
[b] *Shenyang National Laboratory for Materials Science, Institute of Metal Research, Chinese Academy of Sciences, Shenyang, Liaoning, 110016, P. R. China*
† These authors contributed equally to this work.

catalysts, thereby enhancing their activity and stability. For instance, several successful examples using modified Ni-based catalysts, such as NiP,[20] NiSn,[21] and NiAu,[17] have been reported to improve alkane dehydrogenation performance. However, these modified catalysts still face serious scientific challenges, including decreased catalytic performance caused by the loss of accessible Ni active sites and sustained coke accumulation after long-term operation.

C_{60} (fullerene), which was discovered in 1985 and produced on a large scale by the 1990s,[22] has shown intriguing properties in diverse fields, including chemistry, physics, materials science, electronics, and medicine.[23] C_{60} continues to attract considerable scientific interest, particularly due to its emerging roles in energy and catalytic applications.[24–26] Owing to its highly symmetric, π-conjugated structure, C_{60} exhibits excellent electron mobility and low reorganization energy, facilitating the efficient electron transportation.[27,28] Moreover, C_{60} serves as an exceptional electron acceptor, capable of accepting electrons from metal species due to its unique degenerate lowest unoccupied molecular orbital (LUMO) at low energy.[29,30] These characteristics make it a promising candidate for modulating the electronic structure and catalytic performance of Ni centers.[31–33] In contrast, other carbon-based materials such as graphene, carbon nanotubes (CNTs) and fullerene derivatives primarily act through physical dispersion or π–π interactions rather than direct electronic modulation. Graphene and CNTs possess extended π-electron systems that interact weakly with metal orbitals, thus exhibiting limited ability to alter the electron density of Ni atoms.[34–36] C_{60} with its discrete electron-accepting capability can efficiently withdraw electrons from Ni and regulate the d-orbital occupancy, thereby optimizing the adsorption and dehydrogenation behavior of ethylbenzene on Ni sites. This unique electronic interaction distinguishes C_{60} from other carbonaceous modifiers and underpins its effectiveness as an electronic promoter in Ni-based dehydrogenation catalysts.

This work presents a novel and promising strategy to tailor the electronic properties of Ni-based catalysts through introducing C_{60} as the promoter. The hybrid catalyst (C_{60}–Ni/SiO_2), composed of C_{60} promoters and Ni active sites, not only promotes the C–H bond activation during EB DDH but also significantly suppresses carbon deposition. Moreover, comprehensive characterization and mechanistic studies reveal that the electron transfer from Ni active sites to C_{60} modulates the electronic environment of Ni active sites and effectively mitigates sintering and coke formation in EB DDH. To our knowledge, this work introduces C_{60} as the promoter to modify Ni-based catalysts for EB DDH for the first time, offering new avenues for designing high-performance Ni-based catalytic systems.

2. Experimental

2.1. Preparation of materials

The C_{60}–Ni/SiO_2 catalyst was prepared by dissolving 0.10 g of $Ni(NO_3)_2{\cdot}6H_2O$ in deionized water, followed by impregnation onto 1.00 g of nano-sized SiO_2. The resulting mixture was dried at 80 °C for 12 h to obtain the Ni/SiO_2 precursor. Separately, 0.15 g of C_{60} was dispersed in 60 mL of toluene and sonicated for 30 min until the C_{60} was fully dispersed. Subsequently, the C_{60}–toluene solution was added dropwise to the Ni/SiO_2 precursor under continuous mechanical stirring. Then, the resulting mixture was stirred at 60 °C for 12 h. The obtained precipitate was separated by filtration, followed by sequential washing with deionized water and ethanol to remove residual inorganic salts, nitrate ions, and organic species such as toluene and unbound C_{60}. The washed solid was dried under vacuum overnight at 80 °C, and subsequently reduced at 600 °C under a 10% H_2/Ar gas flow for 3 h. The final sample was denoted as C_{60}–Ni/SiO_2. For comparison, C_{60}/SiO_2 and Ni/SiO_2 were prepared following the same procedure while omitting either Ni or C_{60}, respectively.

2.2. Characterization of materials

The morphology and elemental distribution were examined *via* high-resolution transmission electron microscopy (HR-TEM), and energy-dispersive X-ray spectroscopy (EDX) mapping was carried out on an FEI Talos F200S G2 instrument (FEI, USA) operating at 200 kV. XRD patterns were collected on a Bruker D8 ADVANCE diffractometer employing Cu Kα radiation to probe crystal structures. Nitrogen adsorption–desorption isotherms were carried out at 77 K using a Micromeritics ASAP 2020 analyzer, and the specific surface areas (S_{BET}, $m^2\ g^{-1}$) were calculated according to the Brunauer–Emmett–Teller (BET). Thermogravimetric analysis (TG) was conducted on a NETZSCH STA 449 C at 40–900 °C under air or argon atmosphere. A HORIBA LabRam HR800 Raman spectrometer, operated with a 532 nm laser, was employed to collect the Raman spectra. The chemical states of the samples were analyzed *via* X-ray photoelectron spectroscopy (XPS) on an ESCALAB 250 system under ultra-high vacuum (UHV), with a monochromatic aluminum K-alpha (Al Kα) X-ray source with a photon energy of 1486.6 electron volts, a power of 150 watts, and a pass energy of 50.0 electron volts to investigate the chemical states of the samples. Fourier transform infrared (FT-IR) spectra were recorded with a Bruker-V70 spectrometer. For temperature programmed surface reaction (TPSR) experiments, methanol and ethylbenzene (EB) were tested on a Pfeiffer Omnistar mass spectrometer, with a helium flow rate of 15 milliliters per minute, a heating rate of 5 degrees Celsius per minute, and 50 mg of catalyst; the evolutions of EB (mass-to-charge ratio 106), styrene (mass-to-charge ratio 104), and formaldehyde (mass-to-charge ratio 30) were monitored online.

2.3. Measurement of EB DDH activity

The catalytic performance for ethylbenzene direct dehydrogenation (EB DDH) was evaluated in a tubular fixed-bed reactor operating under standard atmospheric

conditions, using helium as the carrier gas under plug-flow conditions. Ethylbenzene was metered into a preheated evaporator using a Cole Parmer (78-9100C) micro-syringe pump and carried by the helium stream into the reactor while maintaining the desired partial pressure. Effluent gases were monitored in real time with an Agilent 7890A gas chromatograph fitted with flame ionization (FID) and thermal conductivity (TCD) detectors. The FID equipped with a methyl silicone HP-5 capillary column was used to achieve separation and measurement of EB and ST, while He, CO, and CO_2 were determined using two Porapak Q packed columns in combination with a molecular sieve 5A column interfaced with the TCD. The overall carbon balance was maintained within 100 ± 5%.

The EB conversion (X_{EB}), the ST selectivity (S_{ST}), and carbon balance ($C_{balance}$) were determined using:

$$X_{EB} = \frac{n_{EB_{in}} - n_{EB_{out}}}{n_{EB_{in}}} \times 100\%$$

$$S_{ST} = \frac{n_{ST}}{n_{EB_{in}} - n_{EB_{out}}} \times 100\%$$

$$C_{balance} = \frac{n_{EB_{out}} + n_{ST} + 1/8 n CO_2}{n_{EB_{in}}} \times 100\%$$

3. Results and discussion

3.1. Chemical and structural features of C_{60}–Ni/SiO_2 catalysts

The C_{60}–Ni/SiO_2 hybrid catalysts were prepared through a simple sequential process involving drying and thermal reduction procedures. Briefly, the SiO_2 support was sequentially impregnated with an aqueous nickel nitrate solution and a C_{60}–toluene dispersed solution, followed by washing with ethanol to remove the residual toluene. The resulting mixture was then dried and thermally reduced at 600 °C in a mixed H_2/Ar gas flow for 2 h to obtain the C_{60}–Ni/SiO_2 catalyst.

Fig. 1a displays the spherical morphology of the SiO_2 support, with particle sizes ranging from 20 to 30 nm. A similar spherical shape morphology was retained in the C_{60}–Ni/SiO_2 catalyst, consistent with that of the Ni/SiO_2 catalyst (Fig. S1). The well-dispersed Ni nanoparticles (NPs) exhibit sizes ranging from 5 to 10 nm, and C_{60} could be observed on the surface of Ni NPs. The selected lattice spacing of 0.204 nm (Fig. 1b) corresponds to the (111) plane of Ni, and an enlarged image (Fig. 1c) shows the diameter of 0.70 nm features corresponding to C_{60} molecules (theoretical diameter: 0.71 nm),[37] confirming that C_{60} is successfully anchored on the surface of the Ni NPs. Furthermore, HAADF-STEM and EDX elemental mapping (Fig. 1d–i) images show uniform distributions of C and Ni elements, further confirming the presence of well-dispersed C_{60} molecules and Ni species on the surface of C_{60}–Ni/SiO_2.

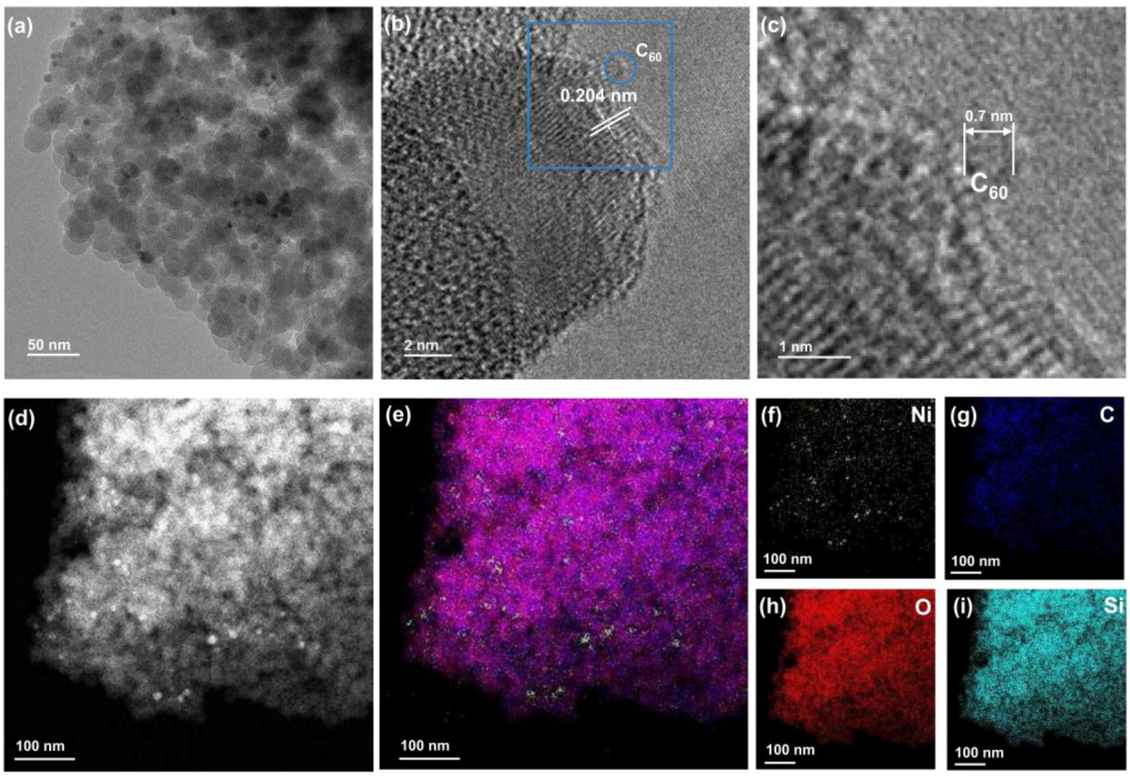

Fig. 1 (a–c) TEM and high-magnification TEM images of C_{60}–Ni/SiO_2. (d–i) HAADF-STEM images and the corresponding EDX mappings of C_{60}–Ni/SiO_2.

The Ni/SiO_2 and C_{60}–Ni/SiO_2 catalysts show similar diffraction peaks corresponding to Ni at approximately 2θ = 44.5°, 51.8° and 76.3°, and no additional specific diffraction peaks could be detected in their XRD patterns (Fig. 2a). The incorporation of C_{60} causes no shift in the diffraction peaks, indicating that the addition of C_{60} does not affect the crystalline structure of Ni.[38] These XRD results are consistent with the observations from TEM images, which reveal that the Ni nanoparticles maintain a similar size distribution and dispersion on the surface of SiO_2 support regardless of C_{60} modification, confirming that C_{60} incorporation does not induce significant morphological changes to the Ni phase. The Raman spectra of C_{60} show two intense signals at approximately 495 cm^{-1} and 1469 cm^{-1}, corresponding to the $A_g(1)$ mode and the $A_g(2)$ mode, respectively, which are recognized as the characteristic vibration signal of C_{60} molecules (Fig. 2b).[39–41] Similarly, the C_{60}–Ni/SiO_2 catalysts also showed typical $A_g(1)$ and $A_g(2)$ Raman bands, confirming the successful incorporation of C_{60} into the C_{60}–Ni/SiO_2 catalysts. The textural properties, including the specific surface area, were measured using N_2 adsorption–desorption isotherms (Fig. 2c). All the samples exhibited adsorption–desorption behaviors similar to typical type IV isotherms according to the IUPAC classifications,[42,43] which are characteristics of mesoporous materials. Capillary condensation occurred between the relative pressures of 0.8 and 1.0, and therefore exhibited the type H_3 hysteresis loop. Pristine SiO_2 exhibited the highest BET surface area (330.5 $m^2\ g^{-1}$), indicative of well-developed mesoporosity. In contrast, the incorporation of C_{60} or Ni reduces the surface area primarily due to partial pore blockage. Interestingly, the C_{60}–Ni/SiO_2 composite maintained a relatively high surface area (121.9 $m^2\ g^{-1}$), suggesting the high dispersion of Ni and C_{60} components. Furthermore, the C_{60} content in the C_{60}–Ni/SiO_2 catalyst was estimated to be approximately 1.5 wt% based on thermogravimetric analysis (TGA) as shown in Fig. 2d. The TGA curve of C_{60}–Ni/SiO_2 under an atmosphere of Ar (Fig. S2) shows that no significant weight loss could be observed below 900 °C, indicating the relatively high thermal stability of the C_{60}–Ni/SiO_2 catalyst under inert conditions.

3.2. Catalytic activity of C_{60}–Ni/SiO_2 catalysts in the EB DDH reaction

After successful construction of the C_{60}–Ni/SiO_2 catalysts, their catalytic performance in the EB DDH reaction, an

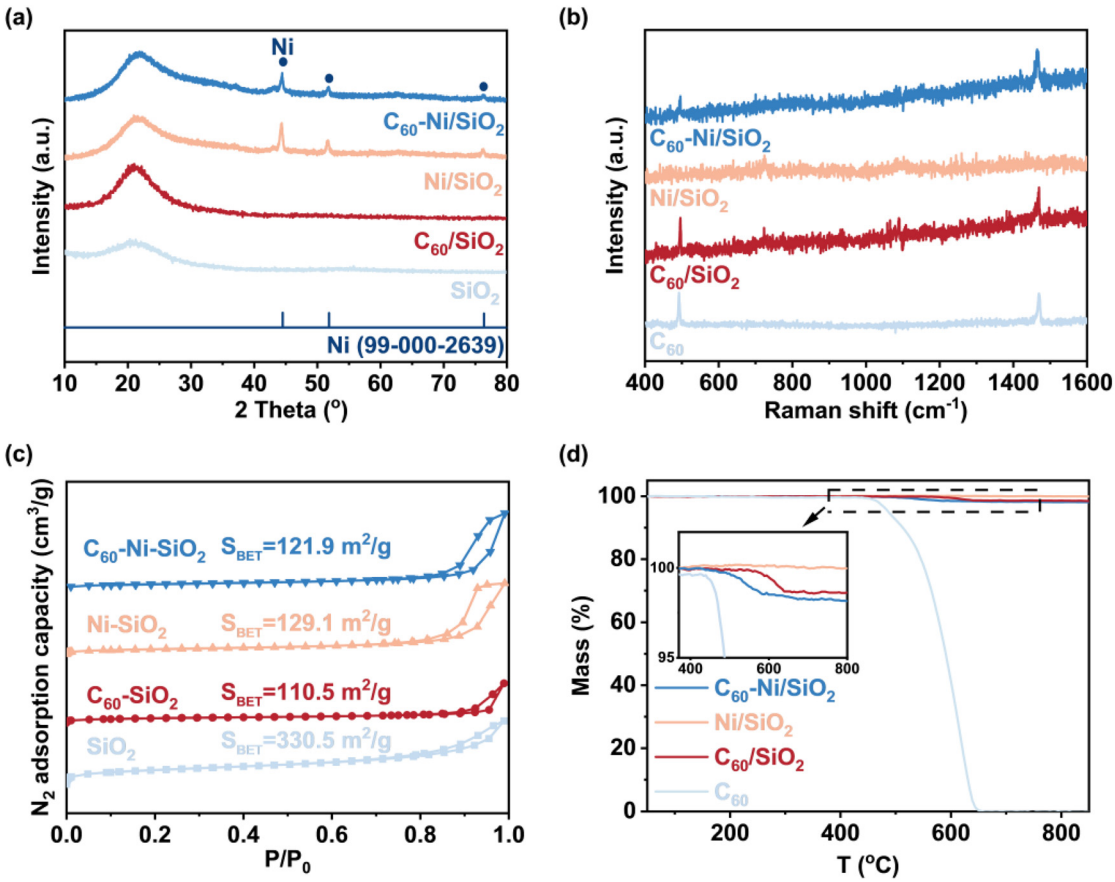

Fig. 2 (a) XRD diffraction patterns of C_{60}–Ni/SiO_2, Ni/SiO_2, C_{60}/SiO_2, and SiO_2. (b) Raman spectra of C_{60}–Ni/SiO_2, Ni/SiO_2, C_{60}/SiO_2 and C_{60}. (c) N_2 adsorption–desorption isotherms of C_{60}–Ni/SiO_2, Ni/SiO_2, C_{60}/SiO_2 and SiO_2. (d) TG profiles under air atmosphere of C_{60}–Ni/SiO_2, Ni/SiO_2, C_{60}/SiO_2 and C_{60} (with the inset showing the magnified view of the dashed-line region).

industrially relevant reaction for ST synthesis, was systematically evaluated.[44,45] The reaction was performed at 550 °C using a feed gas composed of 1% EB balanced in He under ambient pressure. Fig. 3a shows the conversion of EB over time on stream for the C_{60}–Ni/SiO_2 catalyst with Ni/SiO_2 and C_{60}/SiO_2 catalysts for comparison. The C_{60}/SiO_2 catalyst displayed minimal catalytic performance, with a steady state EB conversion of 9.5% (Fig. S3). In contrast, the Ni/SiO_2 catalyst exhibited a carbon balance close to zero, owing to significant carbon accumulation on the catalyst. For comparison, the C_{60}–Ni/SiO_2 catalysts achieved a significantly higher steady EB conversion (30.8%) than both C_{60}/SiO_2 and Ni/SiO_2, highlighting the promotional role of C_{60} and the synergistic effect between C_{60} and Ni in optimizing the catalytic performance of the catalyst in the EB DDH process. TGA and Raman spectra of the spent catalysts (Fig. S9 and S10) demonstrate that carbon deposition on C_{60}–Ni/SiO_2 is significantly lower than that on Ni/SiO_2, confirming the coke-resistant effect of C_{60} modification. The EB conversion over C_{60}–Ni/SiO_2 remained at 25.7% after 18 hours on stream at 550 °C (Fig. 3b), and the selectivity to ST on C_{60}–Ni/SiO_2 kept over 95% even without steam protection, indicating the relatively high stability of the C_{60}–Ni/SiO_2 catalyst. This result indicates that the incorporation of C_{60} successfully inhibits the undesired side reactions. A 60 h long-term stability test was conducted under identical conditions (Fig. S11). The C_{60}–Ni/SiO_2 catalyst maintained an EB conversion of 20–25% and a consistent ST selectivity above 95%, demonstrating its excellent structural robustness and strong resistance to coke formation. Moreover, the catalytic performance of C_{60}–Ni/SiO_2 surpasses the combined activities of Ni/SiO_2 and C_{60}/SiO_2, implying a synergistic interaction between the two components. Because the direct dehydrogenation (DDH) of ethylbenzene is endothermic, elevating the reaction temperature can promote the activation and breaking of the C–H bond. Consequently, EB conversion rises from 18.4% to 49.5% with the reaction temperature rising from 530 to 600 °C (Fig. 3c). However, it should be noted that elevated temperatures also promote the C–C bond cleavage as a secondary reaction, which causes a decrease in ST selectivity from 97.1% to 91.5%. The C_{60}–Ni/SiO_2 catalyst achieved an ST formation rate of 2.7 mmol g^{-1} h^{-1} at 550 °C (Fig. 3d and Table S1), exceeding that of commercial K–Fe (~1.0 mmol g^{-1} h^{-1}) and other reported typical catalysts under the same reaction conditions, demonstrating excellent potential for practical styrene production. For commercial EB dehydrogenation processes, conventional Fe–K catalysts are typically operated under high space velocities and elevated temperatures, delivering long lifetimes but with moderate selectivity.[46] Pt–Sn catalysts exhibit superior selectivity and durability, but they rely on costly and scarce noble metals.[47] In contrast, the C_{60}–Ni/SiO_2

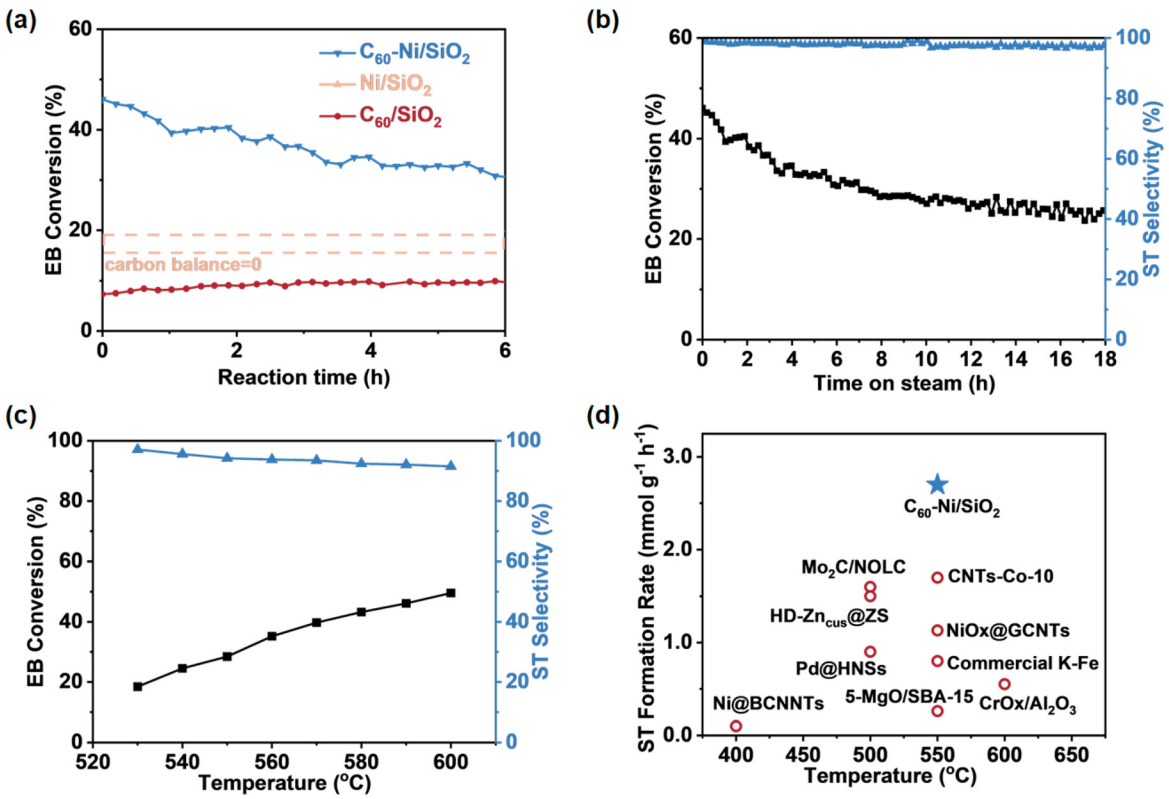

Fig. 3 (a) Conversion of EB over time on C_{60}–Ni/SiO_2, C_{60}/SiO_2, and Ni/SiO_2; (b) EB conversion and ST selectivity of C_{60}–Ni/SiO_2 *versus* reaction time; (c) EB conversion and corresponding ST selectivity over C_{60}–Ni/SiO_2 *versus* reaction temperature. Conditions: 100 mg catalysts, 550 °C, 1.0 kPa EB, total flow 6.12 mL min^{-1} with He as balance gas, carbon balance: 100 ± 5%. (d) Comparisons of the ST formation rates of C_{60}–Ni/SiO_2 with those of other typical reported catalysts at different temperatures.

catalyst, though evaluated at the laboratory scale, bridges the gap between non-noble and noble-metal catalysts, approaching the performance of Pt–Sn systems while maintaining cost efficiency. These results underscore the critical role of C_{60} as an electronic promoter and demonstrate the potential of this non-noble system for sustainable styrene production.

Fig. 4a shows a positive correlation between the EB partial pressure and ST formation rate over the C_{60}–Ni/SiO_2 catalyst, suggesting that EB activation kinetically controls the reaction under these conditions. The reaction order for EB activation was 0.79 (Fig. 4b), implying that EB activation likely serves as the rate-determining step (RDS) over C_{60}–Ni/SiO_2, consistent with other metal catalysts.[44,48–51] The kinetic isotope effect (KIE), quantifying the relative rates of isotopically labeled and unlabeled reactants, is commonly employed to elucidate the kinetic relevance of specific elementary steps. A KIE experiment was conducted on the C_{60}–Ni/SiO_2 catalyst using deuterated EB (D-EB, C_8D_{10}) to further validate the proposed mechanism. As shown in Fig. 4c, the EB conversion over the C_{60}–Ni/SiO_2 catalyst decreases sharply from 24.5% to 13.4%. A reaction rate ratio of 1.82 between EB and deuterated EB ($R_{EB}/R_{D\text{-}EB}$) was observed under steady-state conditions when EB was substituted with D-EB. A similar KIE is also observed for the C_{60}/SiO_2 catalyst (Fig. S4). This result confirms that C–H bond activation and dissociation in EB serve as the RDS under the tested conditions. Furthermore, the KIE results indicate that the activation energy is closely correlated with the capability of the catalysts in activating the C–H bond.[51,52] As shown in Fig. 4d, under conditions where C–H bond activation was the RDS, the apparent activation energies of EB DDH on C_{60}–Ni/SiO_2 and C_{60}/SiO_2 were determined. The activation energy for C_{60}–Ni/SiO_2 was measured at 80 kJ mol^{-1}, significantly lower than that for C_{60}/SiO_2 at 152 kJ mol^{-1}, suggesting that the incorporation of C_{60} substantially lowers the activation energy. This effect highlights the promotional role of C_{60} in C–H bond activation. C_{60}–Ni/SiO_2 demonstrates a lower activation energy than the 105.0 kJ mol^{-1} typically

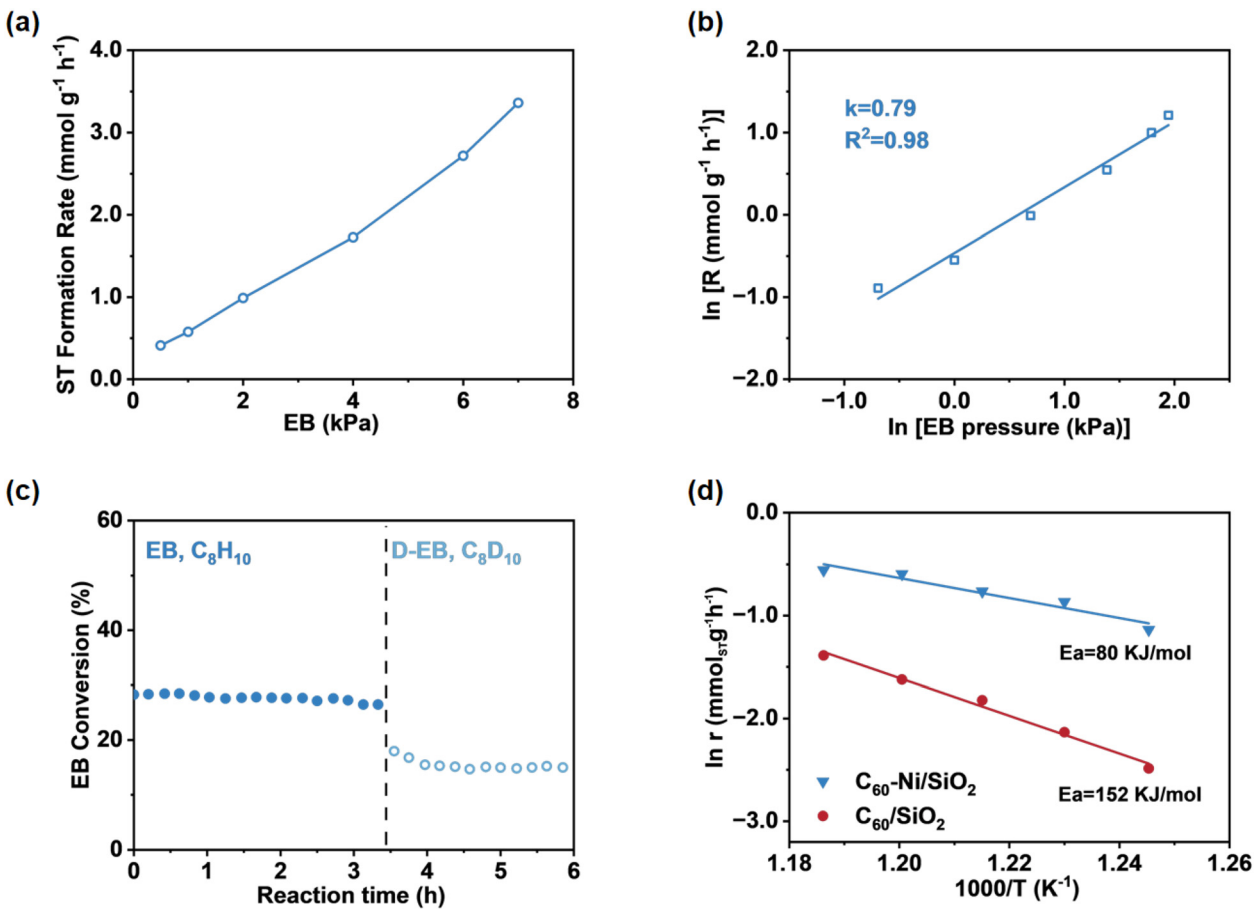

Fig. 4 (a) ST formation rates *versus* partial pressure of EB and (b) corresponding reaction order for the C_{60}–Ni/SiO_2 catalyst. Conditions: 100 mg catalyst, 550 °C, EB partial pressure 0.5–7.0 kPa, total flow 6.12 mL min^{-1} with He as balance gas, carbon balance: 100 ± 5%. (c) Time-on-stream EB conversion over the C_{60}–Ni/SiO_2 catalyst in EB (C_8H_{10})/He and D-EB (C_8D_{10})/He. Conditions: 100 mg catalyst, 550 °C, EB or D-EB partial pressure 1.0 kPa, total flow 6.12 mL min^{-1} with He as balance gas, carbon balance: 100 ± 5%. (d) Arrhenius plots for EB DDH over the C_{60}–Ni/SiO_2 and C_{60}/SiO_2 catalysts. Conditions: 100 mg catalyst, 530–570 °C, EB partial pressure 1.0 kPa, total flow 6.12 mL min^{-1} with He as balance gas, carbon balance: 100 ± 5%.

reported for EB DDH over commercial Fe–K catalysts.[53] These results highlight the unique kinetic advantage of C_{60}–Ni/SiO_2 in facilitating EB dehydrogenation.

3.3. Promotional effect of C_{60} on Ni species in C_{60}–Ni/SiO_2 catalysts

In the Raman spectra of C_{60}, an intense signal is observed at 1469 cm^{-1}, which is the characteristic vibration signal of the C_{60} molecule due to the pentagonal pinch mode $A_g(2)$.[39,40] The Raman spectra of C_{60}/SiO_2 exhibit a superposition of signals from C_{60} moieties, with no discernible shift relative to that of pristine C_{60}, indicating no strong intermolecular interactions between C_{60} and SiO_2. In contrast, a noticeable downshift of the $A_g(2)$ vibration mode is observed in the Raman spectra of C_{60}–Ni/SiO_2, with an approximately 5 cm^{-1} peak shifting from 1469 to 1464 cm^{-1}. As reported, the position of the $A_g(2)$ mode Raman signal reflects changes in the charge state of C_{60};[40,54] therefore, the observed downshift is indicative that there is electron migration from Ni to C_{60}, attributable to the excellent electron-acceptor capability of C_{60}.[54,55] Elemental analysis and surface chemical state identification were carried out *via* X-ray photoelectron spectroscopy. As displayed in Fig. S5, four main peaks corresponding to C 1s, O 1s, Si 1s, and Si 2p XPS signals were identified, consistent with TEM and elemental mapping images. XPS characterization was used to reveal the promotional role of C_{60} by comparing the C_{60}–Ni/SiO_2 and unmodified Ni/SiO_2 catalysts. The binding energy of Ni^0 $2p_{3/2}$ in the XPS spectra of C_{60}–Ni/SiO_2 appears at 856.9 eV, which is +1.0 eV higher than that of Ni/SiO_2 (855.9 eV). A similar positive shift is observed for the Ni^0 $2p_{1/2}$ signal (873.93 → 874.68 eV). These increases in binding energy indicate a decrease of electron density at Ni sites upon C_{60} modification, consistent with the result that partial charge transfers from Ni to the electron-accepting C_{60}. XPS atomic composition analysis reveals nearly identical surface Ni contents (0.49 at%) for C_{60}–Ni/SiO_2 and Ni/SiO_2, confirming that the observed electronic changes arise from interfacial charge redistribution rather than variations of the loading content of Ni. The CO-FTIR results further corroborate this interpretation (Fig. S7). The IR band corresponding to linearly adsorbed CO on Ni/SiO_2 appears at 2026 cm^{-1}, whereas it is centered at 2054 cm^{-1} for C_{60}–Ni/SiO_2, representing a 28 cm^{-1} blueshift. Such a blueshift of the C–O stretching vibration is typically attributed to the weakened π

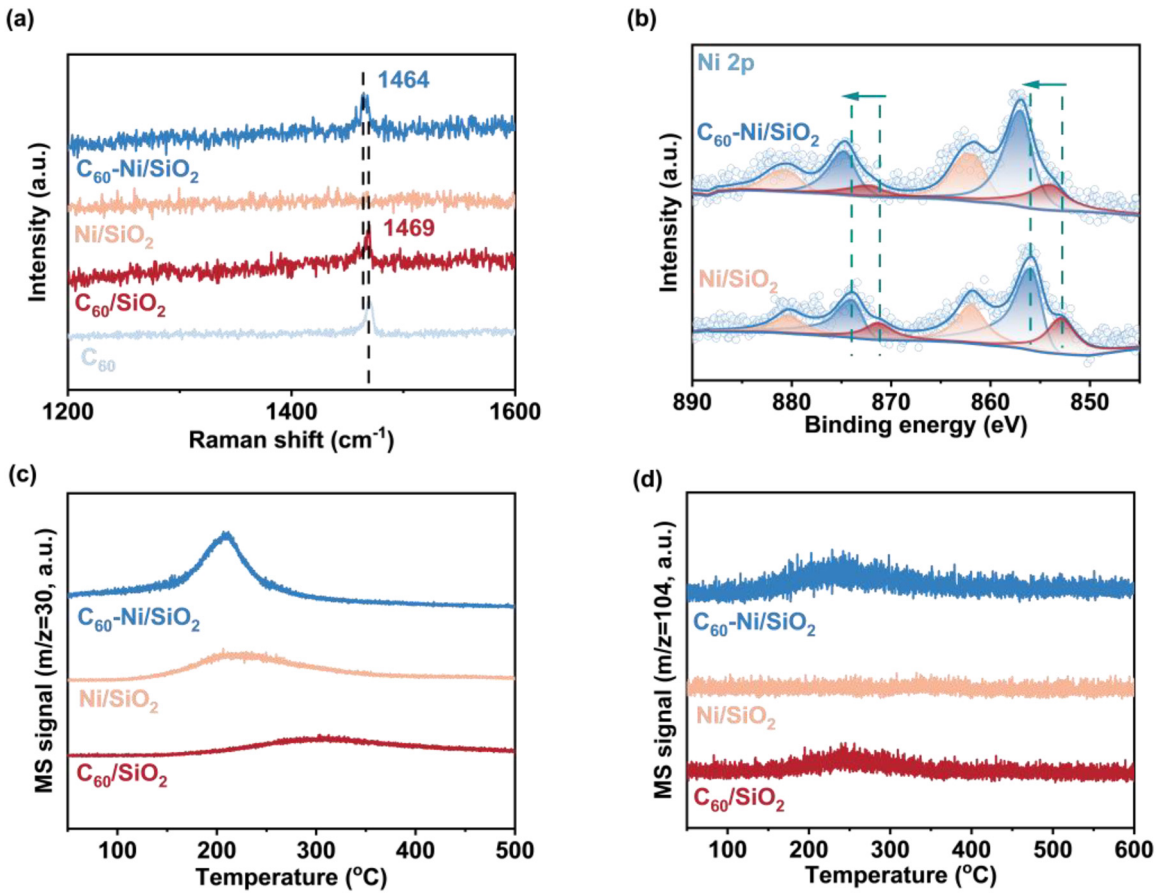

Fig. 5 (a) Raman spectra of C_{60}–Ni/SiO_2, Ni/SiO_2, C_{60}/SiO_2, and C_{60}. (b) Deconvolution of the Ni 2p XPS spectra of C_{60}–Ni/SiO_2 and Ni/SiO_2. (c) MS signals under temperature-programmed reaction conditions of methanol on C_{60}–Ni/SiO_2, Ni/SiO_2, and C_{60}/SiO_2. A heating rate of 5 °C per minute. (d) MS signals of ST under temperature-programmed reaction conditions of EB on the C_{60}–Ni/SiO_2, Ni/SiO_2, and C_{60}/SiO_2 surfaces. A heating rate of 5 °C per minute.

back-donation from d orbitals of the metal to the 2π* antibonding orbital of CO, directly reflecting a reduction in the d-electron density at metal sites.[56–58] The concurrent observation of a 1.0 eV XPS shift and a 28 cm^{-1} CO frequency blueshift is consistent with Raman analysis, thus providing mutually consistent and semi-quantitative evidence that C_{60} modification results in a decreased electron density of Ni species.

Temperature programmed surface reaction (TPSR) experiments with methanol and EB were performed over the C_{60}–Ni/SiO_2 catalyst to elucidate the promotional effect of C_{60} in the EB DDH process.[59] In these TPSR experiments, the selected reactant was first adsorbed onto the catalyst surface, and then purged with helium overnight ensured the removal of physisorbed species. The catalyst was subsequently heated to 500 °C at a rate of 5 °C min^{-1}, while product evolution was continuously monitored by *in situ* mass spectrometry. The analysis focused on formaldehyde (FA) formation from methanol dehydrogenation and styrene (ST) production from EB dehydrogenation as a function of reaction temperature. Methanol was employed as a probe molecule to assess the redox properties of the catalytically active sites on the catalysts.[60] The temperature at which FA desorbed reflected redox ability, with lower desorption temperatures corresponding to higher redox capability.[60,61] The redox capacity is crucial for C–H bond activation during EB DDH. As shown in Fig. 5c, the desorption temperature of formaldehyde on both Ni/SiO_2 and C_{60}–Ni/SiO_2 catalysts was observed at 160 °C. Notably, the C_{60}–Ni/SiO_2 catalyst exhibited a larger peak area than Ni/SiO_2, suggesting that it possesses a higher density of accessible active sites and is less susceptible to carbon deposition. As shown in Fig. 5d and S8, no detectable signals corresponding to EB and ST were observed for Ni/SiO_2 catalysts, possibly due to the strong adsorption of EB on Ni sites. This strong interaction may facilitate deep dehydrogenation and C–C bond dissociation, leading to substantial carbon deposition and a resulting decrease in catalytic performance. In contrast, the signal intensity of EB and ST on C_{60}–Ni/SiO_2 and C_{60}/SiO_2 catalysts is much higher than that on Ni/SiO_2 at temperatures over 200 °C, suggesting more efficient desorption of chemisorbed EB and enhanced ST formation on these C_{60}-based catalysts.

4. Conclusions

In summary, the C_{60}–Ni/SiO_2 catalyst was successfully synthesized through a simple impregnation method, yielding a SiO_2 microsphere structure with Ni and C_{60} uniformly distributed on its surface. Unlike conventional nickel-based catalysts, which normally suffer from carbon deposition, the proposed C_{60}–Ni/SiO_2 catalyst not only suppresses coking, but also exhibits enhanced catalytic activity for EB DDH reactions. The C_{60}–Ni/SiO_2 catalyst exhibited superior catalytic performance in the EB DDH reactions, achieving a remarkable ST selectivity of 99.2% and an ST formation rate of 2.7 mmol g^{-1} h^{-1}. This performance surpassed that of most reported Ni-based catalysts and commercial catalysts under similar reaction conditions. KIE results confirmed that the rate-determining step in EB DDH reactions was the activation of the C–H bond under the catalysis of C_{60}–Ni/SiO_2. The electron-withdrawing properties of C_{60} facilitate the electron transfer from Ni NPs to C_{60} molecular promoters and this transfer is driven by the higher Fermi level of Ni relative to the LUMO of C_{60}, resulting in favorable adsorption and desorption behavior of different intermediates on C_{60}–Ni/SiO_2 compared to traditional Ni-based catalysts. The high catalytic performance of C_{60}–Ni/SiO_2 composites offers a highly effective and promising strategy in the informed design of efficient catalysts in alkane dehydrogenation, offering valuable insights for future informed design of Ni catalysts targeting alkane dehydrogenation.

Conflicts of interest

The authors declare no competing interests.

Data availability

Data are available from the corresponding author upon reasonable request. Supplementary materials include extended characterization of the SiO_2 support and SiO_2-based composites, providing additional structural, textural, and thermal analysis relevant to catalyst performance.

Supplementary information is available. See DOI: https://doi.org/10.1039/d5cy01075f.

Acknowledgements

The authors acknowledge the financial support from the National Natural Science Foundation of China (U23A20545 and 22072163), the Natural Science Foundation of Liaoning Province of China (2024JH3/50100016), the China Baowu Low Carbon Metallurgy Innovation Foundation (BWLCF202113), and the Shccig-Qinling Program.

References

1 Z. Qin, J. Liu, A. Sun and J. Wang, *Ind. Eng. Chem. Res.*, 2003, **42**, 1329–1333.
2 K. Zha, T. Zeng, M. Zhu, C. Wei, L. Song and C. Miao, *Appl. Catal., A*, 2023, **666**, 119372.
3 Z. Zhang, T. Zeng, C. Wei, L. Song and C. Miao, *Mol. Catal.*, 2023, **540**, 113058.
4 Y. Sekine, R. Watanabe, M. Matsukata and E. Kikuchi, *Catal. Lett.*, 2008, **125**, 215–219.
5 N. Mimura, I. Takahara, M. Saito, T. Hattori, K. Ohkuma and M. Ando, *Catal. Today*, 1998, **45**, 61–64.
6 R.-J. Zhang, G.-F. Xia, M.-F. Li, W. Yu, N. Hong and D.-D. Li, *J. Fuel Chem. Technol.*, 2015, **43**, 1359–1365.
7 K. Hou and R. Hughes, *Chem. Eng. J.*, 2001, **82**, 311–328.
8 A. Mohsenzadeh, A. Borjesson, J.-H. Wang, T. Richards and K. Bolton, *Int. J. Mol. Sci.*, 2013, **14**, 23301–23314.
9 J. Carrasco, L. Barrio, P. Liu, J. A. Rodriguez and M. V. Ganduglia-Pirovano, *J. Phys. Chem. C*, 2013, **117**, 8241–8250.

10 F. L. Chan and A. Tanksale, *Renewable Sustainable Energy Rev.*, 2014, **38**, 428–438.
11 B. Abdullah, N. A. Abd Ghani and D.-V. N. Vo, *J. Cleaner Prod.*, 2017, **162**, 170–185.
12 W. Shen, Y. Wang, X. Shi, N. Shah, F. Huggins, S. Bollineni, M. Seehra and G. Huffman, *Energy Fuels*, 2007, **21**, 3520–3529.
13 Z. J. Wang, H. Song, H. Liu and J. Ye, *Angew. Chem., Int. Ed.*, 2020, **59**, 8016–8035.
14 Y. Guo, Y. Li, Y. Ning, Q. Liu, L. Tian, R. Zhang, Q. Fu and Z.-J. Wang, *Ind. Eng. Chem. Res.*, 2020, **59**, 15506–15514.
15 J. J. Sattler, J. Ruiz-Martinez, E. Santillan-Jimenez and B. M. Weckhuysen, *Chem. Rev.*, 2014, **114**, 10613–10653.
16 E. Gianotti, M. Taillades-Jacquin, J. Rozière and D. J. Jones, *ACS Catal.*, 2018, **8**, 4660–4680.
17 Z. Yan and D. W. Goodman, *Catal. Lett.*, 2012, **142**, 517–520.
18 S. Strömberg, M. Svensson and K. Zetterberg, *Organometallics*, 1997, **16**, 3165–3168.
19 C. Massera and G. Frenking, *Organometallics*, 2003, **22**, 2758–2765.
20 G. Zhang, C. Yang and J. Miller, *ChemCatChem*, 2018, **10**, 961–964.
21 H. Wang, H. Wang, X. Li and C. Li, *Appl. Surf. Sci.*, 2017, **407**, 456–462.
22 H. W. Kroto, J. R. Heath, S. C. O'Brien, R. F. Curl and R. E. Smalley, *Nature*, 1985, **318**, 162–163.
23 M. A. Lebedeva, T. W. Chamberlain and A. N. Khlobystov, *Chem. Rev.*, 2015, **115**, 11301–11351.
24 R. Wakimoto, T. Kitamura, F. Ito, H. Usami and H. Moriwaki, *Appl. Catal., B*, 2015, **166**, 544–550.
25 L. Jia, M. Chen and S. Yang, *Mater. Chem. Front.*, 2020, **4**, 2256–2282.
26 J. Chen, J. Luo, E. Hou, P. Song, Y. Li, C. Sun, W. Feng, S. Cheng, H. Zhang and L. Xie, *Nat. Photonics*, 2024, **18**, 464–470.
27 Q. Xie, E. Perez-Cordero and L. Echegoyen, *J. Am. Chem. Soc.*, 1992, **114**, 3978–3980.
28 L. Echegoyen and L. E. Echegoyen, *Acc. Chem. Res.*, 1998, **31**, 593–601.
29 C. A. Reed and R. D. Bolskar, *Chem. Rev.*, 2000, **100**, 1075–1120.
30 L. M. Andersson, *Org. Electron.*, 2011, **12**, 300–305.
31 J. Zheng, L. Huang, C.-H. Cui, Z.-C. Chen, X.-F. Liu, X. Duan, X.-Y. Cao, T.-Z. Yang, H. Zhu and K. Shi, *Science*, 2022, **376**, 288–292.
32 Y. Zhang, X. Peng, H.-R. Tian, B. Yang, Z.-C. Chen, J. Li, T. Zhang, M. Zhang, X. Liang and Z. Yu, *Nat. Chem.*, 2024, **16**, 1781–1787.
33 R. Zhang, Y. Li, X. Zhou, A. Yu, Q. Huang, T. Xu, L. Zhu, P. Peng, S. Song and L. Echegoyen, *Nat. Commun.*, 2023, **14**, 2460.
34 A. Dahal and M. Batzill, *Nanoscale*, 2014, **6**, 2548–2562.
35 J. Li, E. Croiset and L. Ricardez-Sandoval, *Appl. Surf. Sci.*, 2014, **317**, 923–928.
36 K. Miyaura, Y. Miyata, B. Thendie, K. Yanagi, R. Kitaura, Y. Yamamoto, S. Arai, H. Kataura and H. Shinohara, *Sci. Rep.*, 2018, **8**, 8098.
37 J. Guan, X. Zhong, X. Chen, X. Zhu, P. Li, J. Wu, Y. Lu, Y. Yu and S. Yang, *Nanoscale*, 2018, **10**, 2473–2480.
38 J. Wu, S. Wang, Z. Lei, R. Guan, M. Chen, P. Du, Y. Lu, R. Cao and S. Yang, *Nano Res.*, 2021, 1–10.
39 D. Saha and S. Deng, *Langmuir*, 2011, **27**, 6780–6786.
40 F. Leng, I. C. Gerber, P. Lecante, S. Moldovan, M. Girleanu, M. R. Axet and P. Serp, *ACS Catal.*, 2016, **6**, 6018–6024.
41 M. Matus, H. Kuzmany and W. Krätschmer, *Solid State Commun.*, 1991, **80**, 839–842.
42 F. Jing, B. Katryniok, S. Paul, L. Fang, A. Liebens, M. Shen, B. Hu, F. Dumeignil and M. Pera-Titus, *ChemCatChem*, 2017, **9**, 258–262.
43 S. Brunauer, L. S. Deming, W. E. Deming and E. Teller, *J. Am. Chem. Soc.*, 1940, **62**, 1723–1732.
44 W. Liu, B. Chen, X. Duan, K.-H. Wu, W. Qi, X. Guo, B. Zhang and D. Su, *ACS Catal.*, 2017, **7**, 5820–5827.
45 J. Zhang, X. Wang, Q. Su, L. Zhi, A. Thomas, X. Feng, D. S. Su, R. Schlögl and K. Müllen, *J. Am. Chem. Soc.*, 2009, **131**, 11296–11297.
46 E. H. Lee, *Catal. Rev.: Sci. Eng.*, 1974, **8**, 285–305.
47 L. Deng, T. Arakawa, T. Ohkubo, H. Miura, T. Shishido, S. Hosokawa, K. Teramura and T. Tanaka, *Ind. Eng. Chem. Res.*, 2017, **56**, 7160–7172.
48 J. Zhang, D. S. Su, A. Zhang, D. Wang, R. Schlögl and C. Hébert, *Angew. Chem., Int. Ed.*, 2007, **46**, 7319–7323.
49 S. Mao, B. Li and D. Su, *J. Mater. Chem. A*, 2014, **2**, 5287–5294.
50 X. Zhang, X. Dai, Z. Xie and W. Qi, *Small*, 2024, **20**, 2401532.
51 X. Dai, T. Cao, X. Lu, Y. Bai and W. Qi, *Appl. Catal., B*, 2023, **324**, 122205.
52 W. Qi, P. Yan and D. S. Su, *Acc. Chem. Res.*, 2018, **51**, 640–648.
53 J. Sheng, B. Yan, W.-D. Lu, B. Qiu, X.-Q. Gao, D. Wang and A.-H. Lu, *Chem. Soc. Rev.*, 2021, **50**, 1438–1468.
54 A. Talyzin and U. Jansson, *Thin Solid Films*, 2003, **429**, 96–101.
55 X. Zhu, T. Zhang, D. Jiang, H. Duan, Z. Sun, M. Zhang, H. Jin, R. Guan, Y. Liu and M. Chen, *Nat. Commun.*, 2018, **9**, 4177.
56 J. I. Cohen and R. Tobin, *J. Chem. Phys.*, 2018, **148**, 22.
57 J. Lauterbach, M. Wittmann and J. Küppers, *Surf. Sci.*, 1992, **279**, 287–296.
58 Y. Peng, A. Melillo, R. Shi, A. Forneli, A. Franconetti, J. Albero and H. García, *Appl. Catal., B*, 2023, **339**, 123143.
59 H. Huang, F. Tang, J. Sheng, Z. Liu, J. Fan, R.-P. Zhang, D. Wang and A.-H. Lu, *J. Catal.*, 2024, **436**, 115626.
60 M. Badlani and I. E. Wachs, *Catal. Lett.*, 2001, **75**, 137–149.
61 J. Sheng, W.-C. Li, W.-D. Lu, B. Yan, B. Qiu, X.-Q. Gao, R.-P. Zhang, S.-Z. Zhou and A.-H. Lu, *Appl. Catal., B*, 2022, **305**, 121070.